OPEN ACCESS
IOP Publishing
Classical and Quantum Gravity
Class. Quantum Grav. **42** (2025) 085002 (26pp)
https://doi.org/10.1088/1361-6382/adbf62

Spherically symmetric collapse: initial configurations

Elly Bayona[1], **Hernando Quevedo**[1,2,3] **and Miguel Alcubierre**[1,*]

[1] Instituto de Ciencias Nucleares, Universidad Nacional Autónoma de México, Ciudad de México, México
[2] Dipartimento di Fisica and Icra, Università di Roma 'La Sapienza', Roma, Italy
[3] Al-Farabi Kazakh National University, Al-Farabi av. 71, 050040 Almaty, Kazakhstan

E-mail: malcubi@nucleares.unam.mx, elly.bayona@correo.nucleares.unam.mx and quevedo@nucleares.unam.mx

Received 23 October 2024; revised 13 February 2025
Accepted for publication 11 March 2025
Published 1 April 2025

Abstract

The initial state of the spherical gravitational collapse in general relativity has been studied with different methods, especially by using *a priori* given equations of state that describe the matter as a perfect fluid. We propose an alternative approach, in which the energy density of the perfect fluid is given as a polynomial function of the radial coordinate that is well-behaved everywhere inside the fluid. We then solve the corresponding differential equations, including the Tolman–Oppenheimer–Volkoff equilibrium condition, using a fourth-order Runge–Kutta method and obtain a consistent model with a central perfect-fluid core surrounded by dust. We analyze the Hamiltonian constraint, the mass-to-radius relation, the boundary and physical conditions, and the stability and convergence properties of the numerical solutions. The energy density and pressure of the resulting matter distribution satisfy the standard physical conditions. The model is also consistent with the Buchdahl limit

* Author to whom any correspondence should be addressed.

and the speed of sound conditions, even by using realistic values of compact astrophysical objects such as neutron stars.

Keywords: spherical symmetry, perfect fluids,
Tolman–Oppenheimer–Volkoff equation, neutron stars

1. Introduction

The collapse of a mass distribution is of particular importance for analyzing the properties of the gravitational field under extreme conditions. Roughly speaking, the study of the collapse can be divided into two parts, namely, the initial configuration and the dynamics involved in the evolution of that initial configuration. In this work, we will focus on the initial configurations only and leave the dynamics of the collapse for future work. We limit ourselves in this work to the study of spherically symmetric configurations.

Birkhoff's theorem states that the only spherically symmetric vacuum solution of Einstein's equations is the Schwarzschild metric [1]. This facilitates the study of black hole solutions in Einstein's gravity. The case of interior spherically symmetric solutions is more complicated. In general, such interior gravitational fields are assumed to be generated by perfect fluids, and the usual approach to obtain such solutions is to specify *a priori* a particular equation of state (EoS), which is commonly assumed as corresponding to barotropic or polytropic fluids. Although there exist in the literature more than a hundred solutions of this type, unfortunately only a few of them satisfy the most elementary physical conditions [2]. For instance, the celebrated interior Schwarzschild solution [3] with a constant energy density leads to a sound speed that violates the light speed limit. In our opinion, most of the problems related to spherically symmetric perfect-fluid solutions are due to the choice of specific EoS's with the aim of obtaining numerical solutions and, in seldom cases, analytical solutions. In this work, we propose a different approach.

We start with the energy density of the fluid, which we fix as a polynomial function of the radial coordinate with arbitrary coefficients. The main advantage of this approach is that we can fix *a priori* the behavior of the energy density by choosing the values of the free coefficients appropriately. In particular, we can demand that the energy density is a decreasing function with the maximum value at the center of the sphere and with a vanishing value at the radius of the sphere.

It turns out that this simple assumption allows us to construct a model that can be completely controlled with the values of the coefficients of the energy density and the value of the pressure at the center of the sphere. As a result, we obtain several models that can be used to describe the gravitational field of a spherically symmetric mass distribution, satisfying the main physical conditions, namely, the energy density and the pressure are free of singularities and vanish at the exterior of the star, the sound speed satisfies the light speed limit everywhere inside the fluid, and the compactness of the mass distribution satisfies the Buchdahl limit. In addition, we show that the numerical approach used to construct the model satisfies the convergence conditions expected for a numerical solution.

The model we will present consists essentially of a central core surrounded by a layer of dust, the thickness of which can be modified by changing the values of the parameters determining the model. Moreover, we show that the parameters can be fixed using the physical quantities that characterize realistic stars, such as neutron stars. Moreover, we argue that there is observational evidence for the existence of such configurations.

We want to emphasize that our approach is different. Therefore, our aim is not to reproduce results that have been previously obtained by using the standard method of specifying an EoS

a priori. The validity of our approach is demonstrated by showing that the solutions resulting from the integration of the field equations can be used to describe the gravitational field of realistic compact objects. Although our final aim is to investigate the gravitational collapse of realistic compact objects, in this work we focus on the initial configurations only, which we analyze by using the Buchdahl limit.

This work is organized as follows. In section 2, we review the main equations used in general relativity to describe a spherically symmetric perfect fluid and present our proposal for the energy density profile in terms of the radial coordinate. In section 3, we describe the boundary and physical conditions imposed for the model to be physically meaningful. In section 4 we present the numerical solutions that are obtained by solving numerically the Tolman–Oppenheimer–Volkoff (TOV) equation, and describe the details of the main physical quantities that can be obtained from the numerical solutions. In section 5 we show that the model can be used with the physical parameters that characterize canonical neutron stars. Then, in section 6, we test the stability and convergence properties of the model. Finally, in section 7 we review our results and comment on possible applications of our model.

2. Perfect fluids

Consider a perfect fluid described with mass-energy density ρ and pressure p, as measured in its rest frame. The corresponding stress-energy-momentum tensor is given by

$$T_{\mu\nu} = (\rho + p)\, u_\mu u_\nu + p g_{\mu\nu} \,, \tag{1}$$

where $u^\mu = g^{\mu\nu} u_\nu$ are the components of the four-velocity of the fluid element. The main physical property of a perfect fluid is that it corresponds to an idealized matter model because it does not consider physical quantities such as shear stresses, viscosity, or heat conduction, which are characteristics of real fluids.

Consider now a static and spherically symmetric spacetime represented by the general line element

$$\mathrm{d}s^2 = -\mathrm{e}^{2\phi}\mathrm{d}t^2 + \mathrm{e}^{2\psi}\mathrm{d}r^2 + r^2\left(\mathrm{d}\theta^2 + \sin^2\theta \mathrm{d}\varphi^2\right) \,, \tag{2}$$

where ϕ and ψ are functions of the radial coordinate r only. In this case, $u^\mu = \mathrm{e}^{\phi(r)}(\partial_t)^\mu$, so that the four-velocity is normalized as $u^\mu u_\mu = -1$. Then, the independent components of Einstein's equations can be written in geometric units with $G_N = c = 1$ as follows

$$8\pi\rho = \frac{2}{r}\mathrm{e}^{-2\psi}\psi_r + \frac{1-\mathrm{e}^{-2\psi}}{r^2} \,, \tag{3}$$

$$8\pi p = \frac{2}{r}\mathrm{e}^{-2\psi}\phi_r + \frac{\mathrm{e}^{-2\psi}-1}{r^2} \,, \tag{4}$$

$$8\pi p = \mathrm{e}^{-2\psi}\left[(\phi_r)^2 + \phi_{rr} - \phi_r\psi_r + \frac{\phi_r - \psi_r}{r}\right] \,, \tag{5}$$

where $\phi_r = \frac{\partial\phi}{\partial r}$, etc. From (3) we obtain

$$A(r) := \mathrm{e}^{2\psi(r)} = \left(1 - \frac{2m(r)}{r}\right)^{-1} , \qquad m(r) := 4\pi\int_0^r \rho(r')\, r'^2 \mathrm{d}r' \,. \tag{6}$$

where we have introduced the mass function $m(r)$. Then, from (4) we have that

$$\frac{\mathrm{d}\phi}{\mathrm{d}r} = \frac{m(r) + 4\pi r^3 p(r)}{r(r-2m(r))} \,. \tag{7}$$

Finally, using equations (3)–(5), we obtain

$$p_r = -(p+\rho)\,\phi_r\,, \tag{8}$$

which is equivalent to the conservation law $\nabla^\mu T_{\mu\nu} = 0$ and can be represented as the TOV equation,

$$\frac{\mathrm{d}p}{\mathrm{d}r} = -(p(r)+\rho(r))\,\frac{m(r)+4\pi r^3 p(r)}{r(r-2m(r))}\,. \tag{9}$$

For more details, see the review [4].

We see that we have three equations (6), (7) and (9) with four unknown variables, namely, the two metric functions $\phi(r)$ and $A(r) = \mathrm{e}^{2\psi(r)}$, and the two fluid variables $p(r)$ and $\rho(r)$. To search for solutions to this system of equations it is necessary to add an extra equation, which is usually taken to be an EoS of the form $p = p(\rho)$. As mentioned above, this approach leads in many cases to solutions that do not satisfy the physical conditions expected for a realistic spherically symmetric mass distribution. Here, we will proceed in a different way.

2.1. Predetermined density profiles

The alternative approach we propose in this work consists in giving *a priori* the mass-energy density as a function of a radial coordinate in such a way that it satisfies the expected physical conditions, namely, it should be positive and free of divergences in the entire region inside the sphere that contains the mass distribution. Such a profile for the density will guarantee *a priori* that the behavior of the energy density corresponds to that of a realistic astrophysical object. In particular, we can fix the density function as a polynomial of the form

$$\rho(r) = \sum_{i=0}^{n} c_i r^i\,, \tag{10}$$

where c_i represents a series of real constants. For concreteness, we will limit ourselves to the case $n = 4$, which will prove to lead to satisfactory results. We assume that the origin of coordinates is located at the center of the object. This fixes the meaning and the value of one of the coefficients c_i, namely, $c_0 = \rho(r=0), \equiv \rho_\mathrm{c}$. The remaining coefficients will determine the internal structure of the star. For the sake of concreteness, we choose an energy density profile of the form

$$\rho(r) = \rho_\mathrm{c} - c_1 r - c_2 r^2 - c_3 r^3 - c_4 r^4\,. \tag{11}$$

This expression represents the additional equation we need in order to integrate Einstein's equations.

3. Boundary and physical conditions

In order to solve the TOV equations numerically, we will use (11) instead of the typical polytropic EoS. In order to have a regular solution at the origin we assume the density to be a smooth function at the center of the object. This means that we must choose an even profile for the total energy density, i.e.

$$\rho(r) = \begin{cases} \rho_\mathrm{c} - c_2 r^2 - c_4 r^4\,, & r < R \\ 0\,, & r > R\,, \end{cases} \tag{12}$$

with R the radius of the star, which can be defined as the coordinate point where the total energy density is zero $\rho(r=R)=0$, i.e.

$$\rho_{\rm c} = c_4 R^4 + c_2 R^2 \ . \tag{13}$$

This implies a relationship between the central total energy density and the radius of the object. Notice that the radius of the star can also be defined as the location of vanishing pressure, allowing a discontinuity in the density at the surface of the body. This is, for instance, the case of the interior Schwarzschild solution. Our method also allows this possibility by simply assuming that $\rho(R)=\rho_s=const.$ with $p(R)=0$, where ρ_s is the density on the surface. This, however, would lead to a different class of solutions of the TOV equation, i.e. to different models for the interior of the star, which we expect to study in future works. In this work, we will focus on the definition of the radius as the place where the density vanishes and will show that it leads to physically meaningful models.

From the density function (12), we can rewrite now the mass function $m(r)$ as

$$m(r) = \begin{cases} 4\pi r^3 \left[\dfrac{\rho_{\rm c}}{3} - \dfrac{c_2}{5} r^2 - \dfrac{c_4}{7} r^4\right] \ , & r < R \ , \\ 4\pi R^3 \left[\dfrac{\rho_{\rm c}}{3} - \dfrac{c_2}{5} R^2 - \dfrac{c_4}{7} R^4\right] \equiv M \ , & r > R \ . \end{cases} \tag{14}$$

Thus, the metric function $A(r)$ can be expressed in the following manner

$$A(r) = \left(1 - \frac{2m(r)}{r}\right)^{-1} = \begin{cases} \left(1 - 8\pi r^2 \left[\dfrac{\rho_{\rm c}}{3} - \dfrac{c_2 r^2}{5} - \dfrac{c_4 r^4}{7}\right]\right)^{-1} \ , & r < R \\ \left(1 - \dfrac{2M}{r}\right)^{-1} \ , & r > R \ . \end{cases} \tag{15}$$

We will still assume that the perfect fluid is in local thermodynamic equilibrium and isentropic.

As shown in [4], this assumption implies that each fluid cell is in thermodynamic equilibrium and the object is at a maximum of entropy. We also assume that each cell has a fixed number N of particles and the volume is given by $V = N/n$, where n refers to the particle density. Subsequently, we have

$$\mathrm{d}e = -p\,\mathrm{d}\left(\frac{1}{\rho_0}\right) = \frac{p}{\rho_0^2}\,\mathrm{d}\rho_0 \ . \tag{16}$$

Here, $e = U/M$ is the internal specific energy, where U is the internal energy, M the total mass of the object, and ρ_0 is the rest mass energy density. Then, we have two new quantities that describe the state of the fluid and are related to the total energy density through

$$\rho(r) = \rho_0(r)\,(1 + e(r)) \ . \tag{17}$$

Calculating the derivative of (17), and matching it with (16), we obtain

$$\frac{\mathrm{d}\rho_0}{\mathrm{d}r} = \frac{\rho_0}{[p(r) + \rho(r)]}\,\frac{\mathrm{d}\rho}{\mathrm{d}r} \ , \tag{18}$$

where the total energy density derivative is clearly given by

$$\frac{\mathrm{d}\rho}{\mathrm{d}r} = \begin{cases} -2r\left(c_2 + 2c_4 r^2\right) \ , & r < R \ , \\ 0 \ , & r > R \ . \end{cases} \tag{19}$$

Therefore, (17) and (18) are two additional equations that are needed in order to find the thermodynamic quantities $\rho_0(r)$ and $e(r)$.

In summary, our system of equations contains two metric functions ($\phi(r)$ and $A(r)$, or equivalently $m(r)$), and four thermodynamic quantities ($p(r)$, $\rho(r)$, $\rho_0(r)$, $e(r)$), which should be solved using equations (6), (7), (9), (12), (17) and (18).

Another important physical quantity is the speed of sound inside the fluid, v_s, which is defined as

$$v_s^2 = \frac{\partial p}{\partial \rho} \,. \tag{20}$$

For the numerical estimation of this quantity, we integrate the TOV equations to obtain $p = p(r)$ and use the expression (12) to evaluate $\rho = \rho(r)$, so that for different values of r we can calculate

$$v_s^2 = \frac{\Delta p}{\Delta \rho} \,, \tag{21}$$

up to the second order. For the sound speed to be physical, we demand that it satisfies the light speed limit, i.e. $v_s^2 < 1$.

3.1. Behavior at $r = 0$

From a physical (and numerical) point of view, it is important to examine the behavior of certain quantities and differential equations that may be diverging at the center of the object $r = 0$. For example, at $r = 0$ the metric function $A(r)$ is finite and tends to 1, as can be seen from the right-hand side of equation (15). Moreover, by replacing the mass function (14) in equations (9) and (19) in (18), and evaluating at $r = 0$, one obtains:

$$\left.\frac{\mathrm{d}p}{\mathrm{d}r}\right|_{r=0} = 0 \,, \qquad \left.\frac{\mathrm{d}\rho_0}{\mathrm{d}r}\right|_{r=0} = 0 \,. \tag{22}$$

Equation (22) is valid if the pressure p and the density ρ_0 remain finite at $r = 0$. This is a consequence of the theorem proved in [4], stating that the solution of the TOV equations satisfies these requirements and is unique.

Furthermore, it is possible to find the analytical value of the speed of sound at the center of the object. To this end, we first replace the value of the function $m(r)$ from equation (14) in the TOV equation (9). We then use the expression for the derivative of the total energy density (19) and the TOV equation (9) and, finally, use the chain rule to obtain

$$v_s^2|_{r=0} = \left[\frac{\mathrm{d}p}{\mathrm{d}r}\left(\frac{\mathrm{d}\rho}{\mathrm{d}r}\right)^{-1}\right]_{r=0} = \frac{2\pi}{c_2}\,(p_\mathrm{c} + \rho_\mathrm{c})\left(p_\mathrm{c} + \frac{\rho_\mathrm{c}}{3}\right) \,, \tag{23}$$

which should also satisfy the light-speed limit

$$\frac{2\pi}{c_2}\,(p_\mathrm{c} + \rho_\mathrm{c})\left(p_\mathrm{c} + \frac{\rho_\mathrm{c}}{3}\right) < 1, \tag{24}$$

where p_c and ρ_c are the central pressure and density, i.e. at $r = 0$. As a result, the expression for the total energy density (12) ensures that our system of equations behaves properly at $r = 0$.

3.2. Additional physical conditions

We will impose two additional physical conditions in order to obtain realistic configurations. The first condition is related to the stability of the object and is known as the Buchdahl limit, which states that the compactness ratio of the object should be bounded from above, i.e.

$$\frac{2m(r)}{r} < \frac{8}{9}\,. \tag{25}$$

Although this limit was first shown for incompressible spheres [5], it can be generalized to include a wide class of physically reasonable equations of state [4].

Notice that the Buchdahl condition is assumed to obtain stable configurations that could describe the gravitational field of realistic astrophysical bodies. However, if we are interested in configurations that can undergo a gravitational collapse, the Buchdahl limit represents a useful tool to control the beginning of the collapse. In fact, if we assume a compactness ratio such that $2m(r)/r \geqslant 8/9$, the initial condition for a gravitational collapse is guaranteed.

A consequence of imposing the Buchdahl limit (25) is the fact that the metric function $A(r)$ does not diverge, i.e.

$$A(r) = \left(1 - \frac{2m(r)}{r}\right)^{-1} < 9\,, \tag{26}$$

which is a condition that must be taken into account when solving the system of equations that determine the spherical configurations.

The second physical condition that we will impose states that

$$e_{\rm c} = \frac{\rho_{\rm c}}{\rho_{0_{\rm c}}} - 1 \geqslant 0\,, \tag{27}$$

which means that the specific internal energy must be positive, implying that the central total energy density must be greater than the central rest energy density.

4. Numerical solutions

To solve the problem discussed in the previous sections, we should consider two important aspects. The first concerns the metric function $\phi(r)$. If we find the radial dependence of the mass function $m(r)$ and the pressure $p(r)$, we can then easily find the solution for $\phi(r)$ by simple integration using (7). We will use this procedure to find the explicit behavior of $\phi(r)$.

The second aspect is related to the free parameters of the problem. To determine the energy density profile (12), it is necessary to specify three parameters, namely the central energy density $\rho_{\rm c}$ and the two coefficients c_2 and c_4. Furthermore, to solve the TOV differential equations (9) and (18) it is necessary to fix the central pressure $p_{\rm c}$ and the central internal specific energy $e_{\rm c}$. Consequently, we need to fix five parameters before solving the problem numerically. It turns out that there are several possibilities that lead to physically reasonable solutions. In table 1 we present the values of the parameters for the two representative models that we will analyze in detail.

Finally, as previously mentioned, we intend to utilize the results of the present work as initial configuration for studying the collapse of a spherically symmetric mass distribution, for which we will use the Ollinsphere code that uses the Baumgarte–Shapiro–Shibata–Nakamura formulation [6–8] adapted to spherical symmetry [9]. This code has been described before for example in [10, 11]. Therefore, the numerical code developed here has been adapted to the requirements of the OllinSphere code. To solve the TOV differential equations, we will use a fourth-order Runge–Kutta method [12].

Table 1. Two sets of parameters necessary for integrating the TOV equations. Model 1 leads to a central sound speed $v_s|_{r=0} = 0.76$ and radius $R = 0.9$, while for model 2 we obtain $v_s|_{r=0} = 0.92$ and $R = 1.3$.

Parameter	Model 1	Model 2
Central rest energy density ρ_c	0.088 04	0.142 44
Central internal energy e_c	0.05	0.11
Central pressure p_c	0.01	0.02
Constant c_2	0.041 79	0.082 59
Constant c_4	0.083	0.001

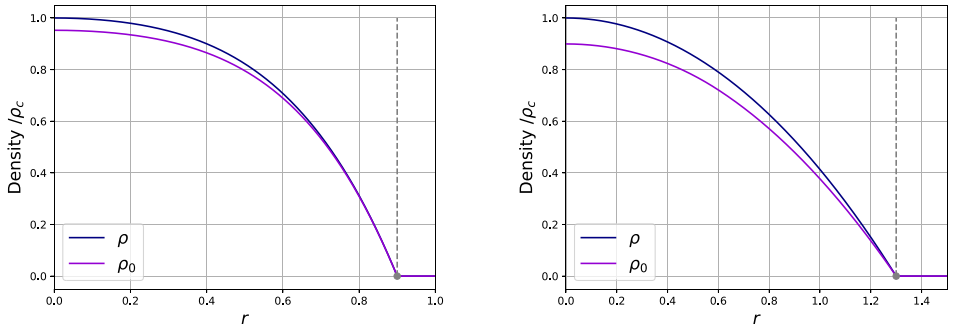

(a) Energy densities for model 1, with radius $R = 0.9$.

(b) Energy densities for model 2 of, with radius $R = 1.3$.

Figure 1. Rest mass and total energy density profiles $\rho_0(r)$ and $\rho(r)$ for the two models presented in table 1. The radius of the object is represented by the dashed gray vertical line.

We now present the main results of the numerical integration. In figure 1, we plot the profile of the total and rest mass energy densities. In both cases we observe that the energy densities are decreasing functions of the radial coordinate r, reaching the zero-value at the radius of the object $r = R$. The pressure profile $p(r)$ is presented in figure 2. It turns out that in both cases the pressure becomes zero at a radial distance smaller than the radius of the object. For model 1 we find that the pressure becomes zero at a radius $r_{p1} = 0.82$, while for model 2 this happens at $r_{p2} = 0.6$. This means that the spherical configuration consists of a central core surrounded by a layer of dust with zero pressure, which extends from $r = r_p$ to $r = R$. In models 1 and 2 the thickness of this layer is 0.08 and 0.7, respectively. Interestingly, the dust layer is always present for all the explored choices of parameters that satisfy the physical conditions and, remarkably, such configurations have been observed in the Universe. For instance, Pleiades stars are surrounded by dust, which, although unrelated to the stars themselves and originating instead from the interstellar cloud, still exists and interacts with the stars. Another case involves supergiant stars that shed mass, creating dust layers [13]. Red giants are also frequently enveloped by a dust shell formed from material ejected from their outer layers. This phenomenon is discussed in [14], where the authors investigate the origin of the dust layer

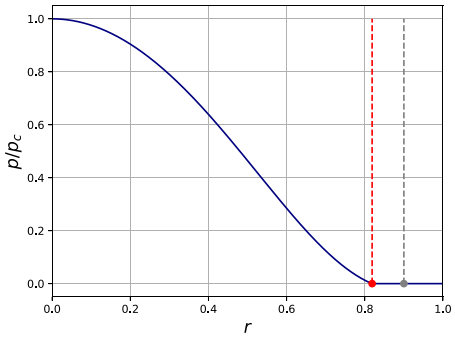

(a) Pressure for model 1 ,with zero-pressure radius $r_{p1} = 0.82$.

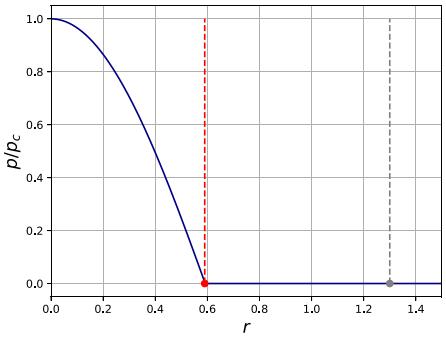

(b) Pressure for model 2, with zero-pressure radius $r_{p2} = 0.6$.

Figure 2. Pressure profiles $p(r)$ for the two models presented in table 1. The radius of the object is again represented by dashed gray vertical lines, while the radius at which the pressure becomes zero is denoted by dashed red vertical lines.

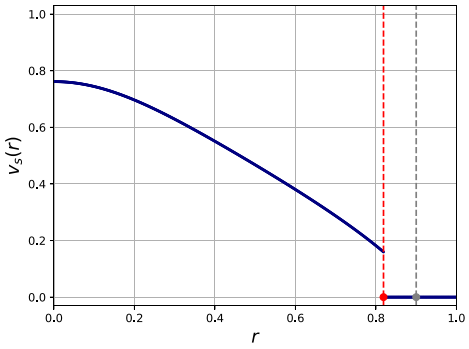

(a) Sound speed for model 1.

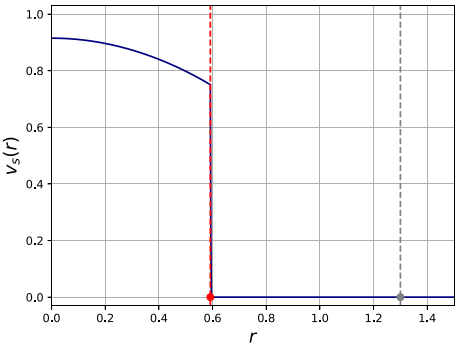

(b) Sound speed for model 2.

Figure 3. Sound speed $v_s(r)$ for the two models presented in the table 1. The radius of the star is shown as a gray vertical line.

around luminosity class III red giants. Similarly, in the case of main-sequence stars, a shell around the star α Lyrae was discovered in 1983 [15].

The speed of sound for both models is shown in figure 3. The maximum values are $v_s = 0.76$ for model 1 and $v_s = 0.92$ for model 2 and are reached at the center of the object in both cases. Notice that even when the parameters of the table 1 were forced to satisfy the speed of light limit only at the center of the object, this limit is valid for all values of the radius. Moreover, the speed of sound decreases monotonically as expected from a physical viewpoint. Therefore, in both cases, the speed of light limit is completely satisfied. Additionally, note that both models exhibit a discontinuity at the point where the pressure vanishes.

On the other hand, from equation (17) we can obtain the specific internal energy that is shown in figure 4. As can be observed from the plots, there seems to be a small peak in the internal energy density as we approach the surface of the star (see inset in the plots). This peak is caused by numerical error, and it appears because as we approach the star's radius R,

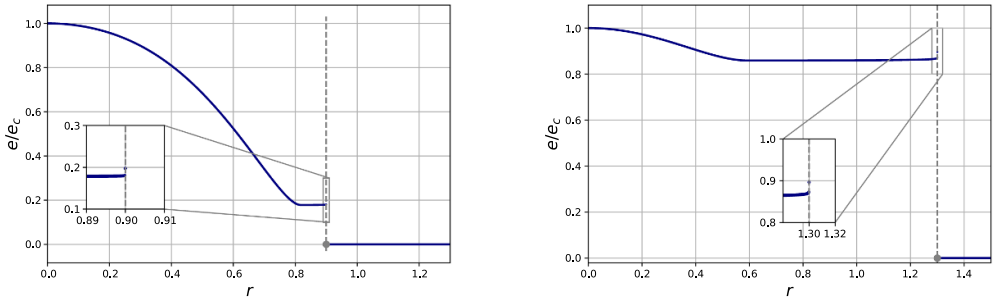

(a) Specific internal energy for model 1.

(b) Specific internal energy for model 2.

Figure 4. Specific internal energy profile $e(r)$ for the models presented in table 1.

both the energy density and rest mass density approach zero, $\rho/\rho_0 \to 0/0$. However, $e(r)$ never diverges and the peak becomes smaller as we increase the numerical resolution. For $r > R$ we simply take $e = 0$ outside the object since the specific internal energy density must vanish in the external Schwarzschild solution.

Additionally, we can find an effective EoS by plotting the pressure as a function of the total energy density. The resulting graph is shown in figure 5. This graph clearly illustrates the behavior at the core of the object. In the dust region, the EoS is simply $p = 0$. The effective EoS corresponding to model 2 (see figure 5(b)) is equivalent to a barotropic EoS. Below, we will see that the barotropic factor satisfies the requirements following imposing the causality condition of the speed of sound. This shows that model 2 is physically meaningful. As for the effective EoS of model 1, we see in figure 5(a) a curve that resembles the behavior of a polytropic EoS. To verify this idea, in figure 6, we plot a particular polytropic EoS and several effective EoSs that follow the approach proposed in this work. In general, we see that for an entire set of parameters c_2 and c_4, it is possible to reproduce the approximate behavior of a polytropic EoS. We conclude that compact objects corresponding to model 1 can be interpreted as having an internal polytropic-like structure. On the other hand, the model 2 can be used to describe barotropic-like compact objects.

Figure 7 shows the barotropic function $\omega(r) = p(r)/\rho(r)$, which is the ratio between the pressure and the total energy density. The most common models used to study the interior solutions of spherically symmetric objects are based on barotropic or polytropic EoSs. In the barotropic case, the ratio between pressure and density remains constant, whereas in the polytropic case, the two quantities are related through a monotonic power-law relationship. In this study, we observe a behavior more akin to the polytropic case than to the barotropic case. The key point to emphasize here is that this behavior is derived from the numerical solution obtained from the field equations, and is no longer an assumption.

Finally, the mass function $m(r)$ is presented in figure 8, and the metric functions $\mathrm{e}^{2\phi(r)}$ and $A(r) = \mathrm{e}^{2\psi(r)}$ in figures 10 and 9, respectively. In both cases, the Buchdahl condition (26) is clearly satisfied, as evidenced by the fact that the maximum value of the metric function $A(r)$ is less than 9. The metric function $g_{00} = \mathrm{e}^{2\phi(r)}$ is also interesting, as it represents the gravitational time dilation for a stationary observer, $\mathrm{d}\tau = \mathrm{e}^{\phi(r)}\mathrm{d}t$, and it also plays the role of the Newtonian gravitational potential. Notice that for model 1 we already have $\mathrm{e}^{2\phi(r=0)} \simeq 0.5$ at the center of the star, while for model 2 we have $\mathrm{e}^{2\phi(r=0)} \simeq 0.02$ indicating an extremely

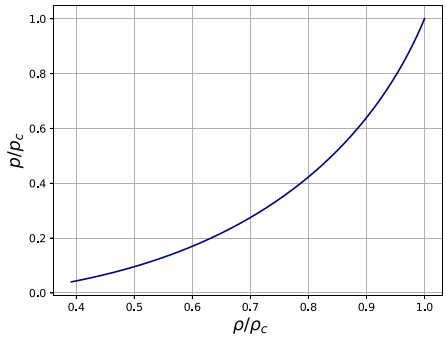

(a) Pressure as a function of the total energy density for model 1.

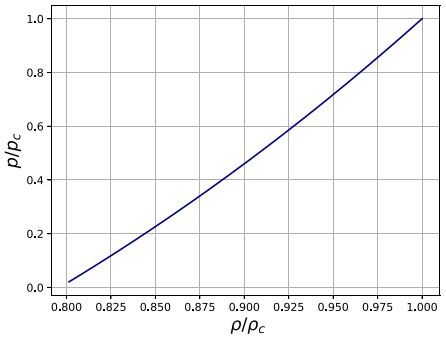

(b) Pressure as a function of the total energy density for model 2.

Figure 5. Effective equation of state. Pressure p as a function of the total energy density ρ for the two models presented in table 1.

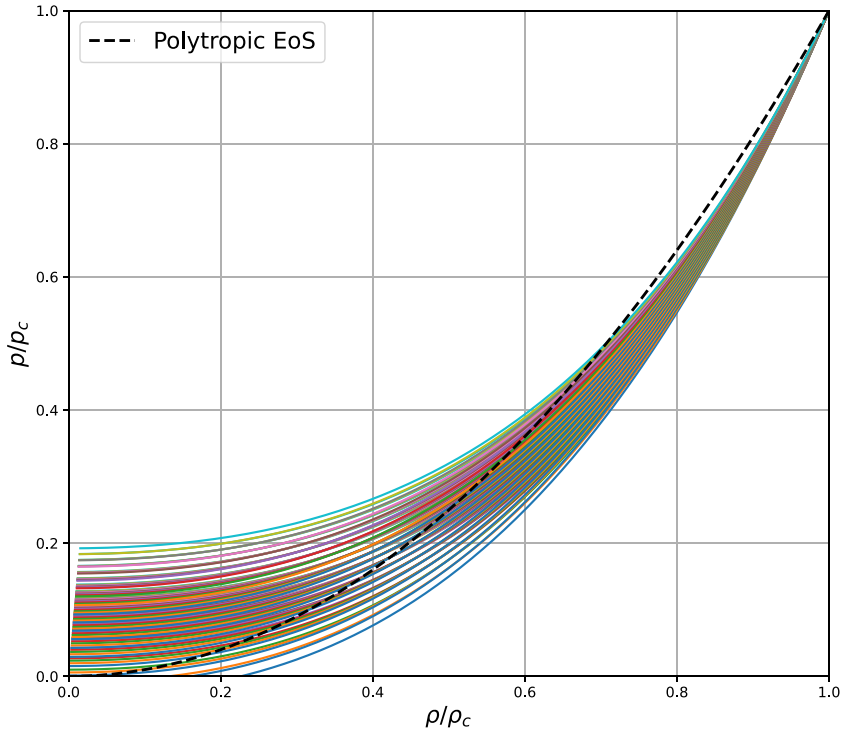

Figure 6. Effective equations of state for parameter values in the interval $c_2 \in [1.75 \times 10^{-5}, 2.01 \times 10^{-5}$ and $c_4 \in [10^{-12}, 10^{-7}]$. The dashed black curve represents a polytropic EoS with $\gamma = 2$ *y* $\kappa = 100$.

large gravitational time dilation factor. Furthermore, it should be noted that the metric functions match the well-known Schwarzschild solution outside the star's radius (shown as a dotted blue line in the plots).

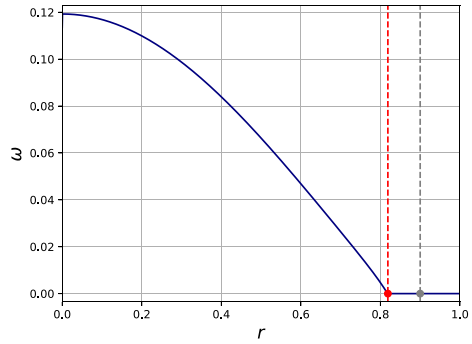

(a) Barotropic function for model 1.

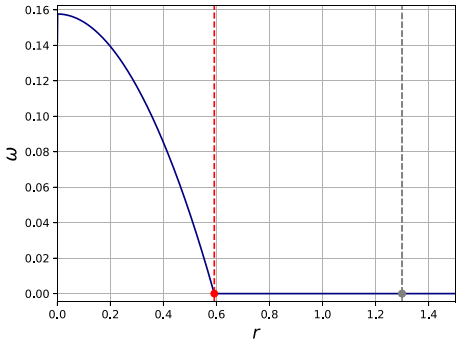

(b) Barotropic function for model 2.

Figure 7. Ratio between the pressure and the total energy density $\omega(r) = p(r)/\rho(r)$ for the two models presented in table 1. The radius of the object is shown in gray.

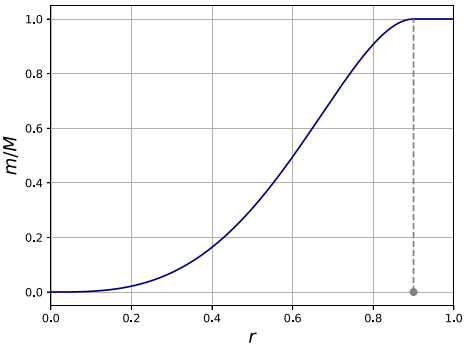

(a) Mass function for model 1.

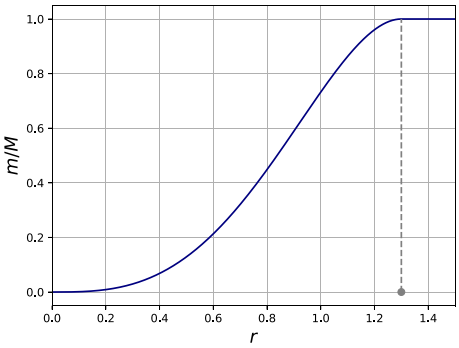

(b) Mass function for model 2.

Figure 8. Mass function $m(r)$ for the two models presented in table 1. The radius of the object is shown in gray.

5. Case of canonical neutron stars

In this section, we will see if our model of a spherically symmetric mass distribution can be applied to the case of realistic neutron stars. Consider first a sphere of uniform density with mass $M = 1.4\,\mathrm{M}_\odot$, radius $R = 12\,\mathrm{km}$, and volumetric mean density $\bar{\rho}_0 = 10^{17}\,\mathrm{kg\,m^{-3}}$, which is the density of an atomic nucleus. The above parameters are used to characterize canonical neutron stars (see for example [16]). Moreover, we assume that the central pressure is also determined by the pressure of an atomic nucleus, which is around $5.24 \times 10^{33}\,\mathrm{N\,m^{-2}}$.

By using the above information, it is possible to fix three of our five free parameters. First, the radius of the star is set to $R = 12\,\mathrm{km}$. Second, in order to find the rest energy density we use the volumetric density in the following way: $\rho_{0_\mathrm{c}} = c^2\bar{\rho}_0 = 3.48 \times 10^{34}\,\mathrm{J\,m^{-3}}$, which corresponds to $\rho_{0_\mathrm{c}} = 2.87 \times 10^{-4}\,\mathrm{km^{-2}}$ in geometric units. Finally, the pressure $p_\mathrm{c} = 5.24 \times 10^{33}\,\mathrm{N\,m^{-2}}$ becomes $p_\mathrm{c} = 4.33 \times 10^{-5}\,\mathrm{km^{-2}}$ in geometric units.

With this set of fixed parameters we can now find the interval of values for c_2 and c_4 that are consistent with the physical requirements of sections 3.1 and 3.2. As a result, we obtain the

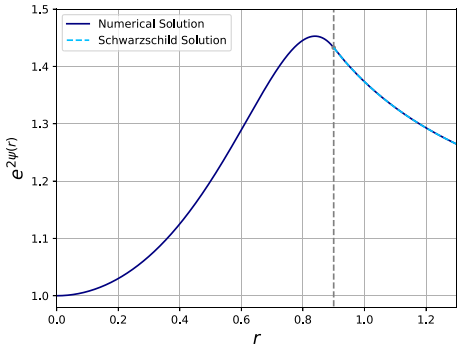

(a) Metric function $A(r)$ for model 1.

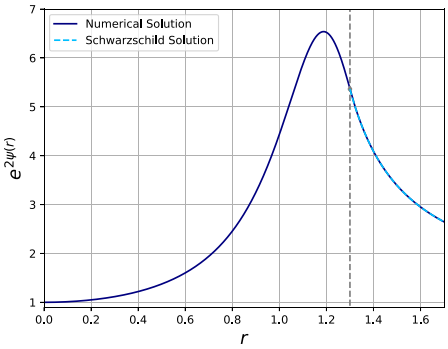

(b) Metric function $A(r)$ for model 2.

Figure 9. Radial metric function $A(r) = \mathrm{e}^{2\psi(r)}$ for the two models presented in table 1. The radius of the object is shown in gray.

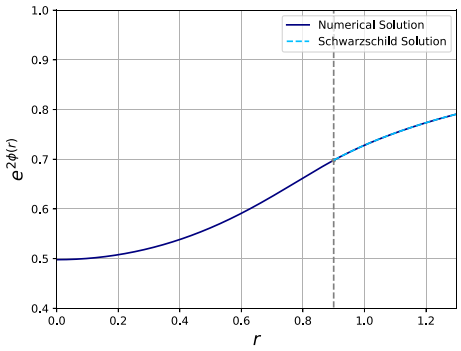

(a) Metric function $e^{\phi(r)}$ for model 1.

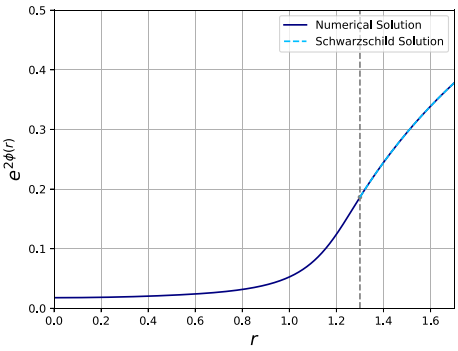

(b) Metric function $e^{2\phi(r)}$ for model 2.

Figure 10. Metric function $\mathrm{e}^{2\phi(r)}$ for the two models presented in table 1. The radius of the object is shown in gray.

regions presented in figure 11. The information about the sound speed is shown in figure 11(a). Additionally, figure 11(b) presents the thickness of the object's central core where the pressure is non-zero, i.e. the 'core radius'. Specifically, we have chosen to represent the thickness of the central core ignoring the dust layer. In particular, we can observe that the core radius has larger values when the sound speed at the center is smaller.

We will now consider the two specific models presented in table 2. The numerical solution of the equations is represented in the following set of plots, where we can see that they have a behavior similar to the models presented in the previous section. Figure 12 illustrates the behavior of the total energy density and the rest mass energy density for the parameters given in table 2. We observe a smooth and monotonically decreasing behavior for the densities, which vanish at the radius of the star as required.

The dependency of the pressure p on the radial coordinate r is shown in figure 13. The pressure vanishes at $r_{p1} = 10.02\,\mathrm{km}$ for model 3, and at $r_{p2} = 5.05\,\mathrm{km}$ for model 4. Thus, in both cases, the central core is surrounded by a layer of dust where the pressure vanishes. The layer of dust has a thickness of 1.98 km and 6.95 km in models 3 and 4, respectively.

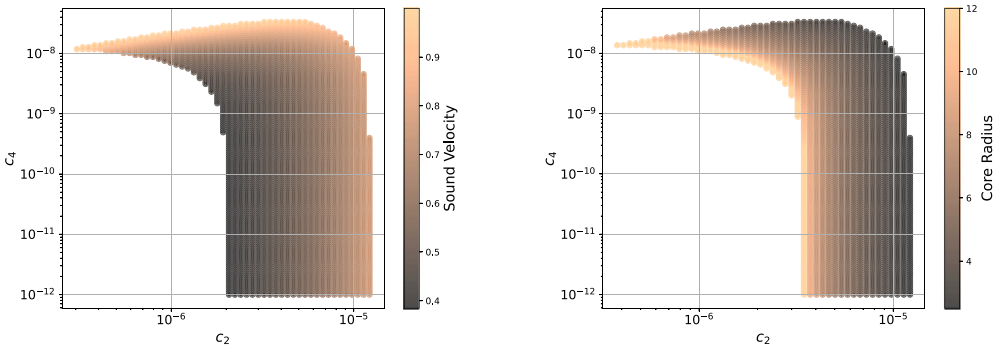

(a) Sound speed for the allowed cases. (b) Core radius for the allowed cases.

Figure 11. Values of the parameters c_2 and c_4 that meet the physical requirements established in subsection 3.2. The color map of the subplot (a) shows the sound speed at the center of the object, while the color map of the subplot (b) shows the size of the core radius of the numerical solution.

Table 2. Two sets of parameters necessary for integrating the TOV equations with radius $R = 12\,\text{km}$. Model 3 leads to a central sound speed $v_s|_{r=0} = 0.84$, while for model 4 we obtain $v_s|_{r=0} = 0.64$. In both cases the central rest energy density is $\rho_{0_c} = 2.87 \times 10^{-4}\,\text{km}^{-2}$ and the central pressure is $p_c = 4.33 \times 10^{-5}\,\text{km}^{-2}$.

Parameter	Model 3	Model 4
Constant c_2	8.55×10^{-7}	4.67×10^{-6}
Constant c_4	1.59×10^{-8}	9.46×10^{-9}

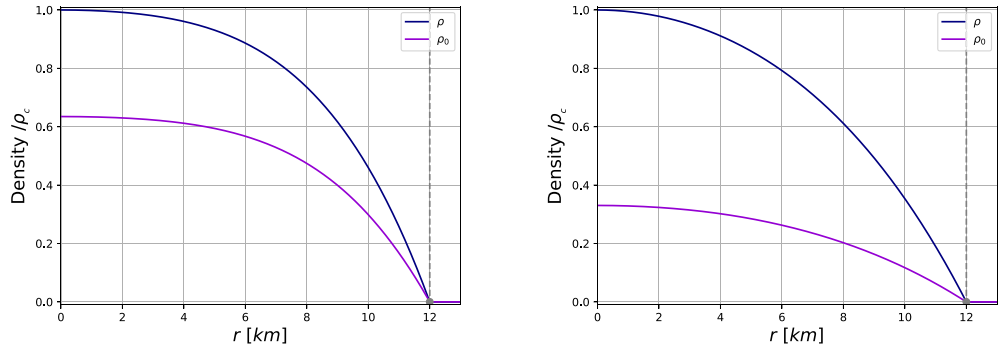

(a) Energy densities for model 3. (b) Energy densities for model 4.

Figure 12. Total and rest mass energy densities profiles $\rho(r)$ and $\rho_0(r)$ for the two models presented in table 2. The radius of the star is represented by the vertical gray line.

The specific internal energy profile $e(r)$ is presented in figure 14. As before, as we approach the star's radius R there is a small peak in $e(r)$ caused by a numerical error coming from the fact that both ρ, and ρ_0 vanish there, but the internal energy remains finite.

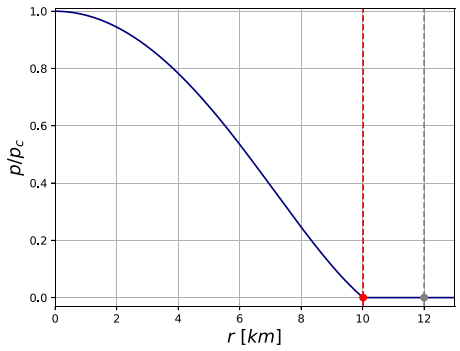

(a) Pressure for model 3. The radius of zero-pressure is $r_{p1} = 10.02\ km$.

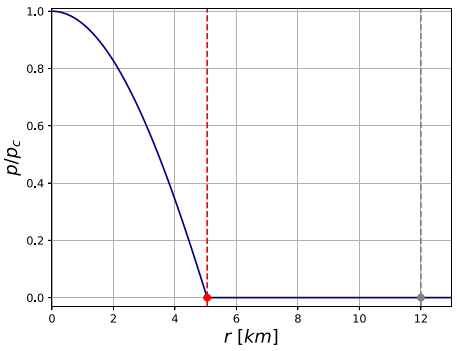

(b) Pressure for model 4. The radius of zero-pressure is $r_{p2} = 5.05\ km$.

Figure 13. Pressure profile $p(r)$ for the two models presented in table 2. The radius of the star corresponds to the vertical gray line, and the radius where the pressure vanishes corresponds to the vertical red line.

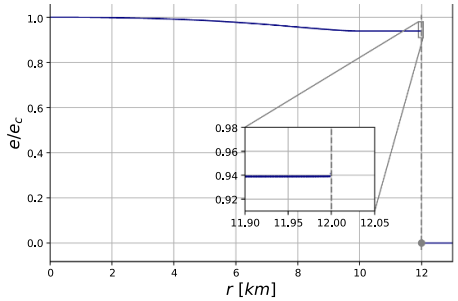

(a) Specific internal energy for model 3.

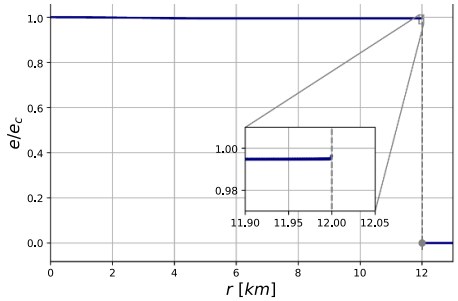

(b) Specific internal energy for model 4.

Figure 14. Specific internal energy profile $e(r)$ for the models presented in table 2. The radius of the star is shown as a gray vertical dashed line.

The speed of sound for both models is shown in figure 15. Its maximum value is attained at the center of the star, with $v_s = 0.84$ for model 3 and $v_s = 0.64$ for model 4. In both models, the speed of sound decreases monotonically and the speed of light limit is fully satisfied, as expected.

As before, we can derive an EoS by plotting the pressure as a function of the total energy density for the core. This is shown in figure 16, where we observe that the pressure is a monotonically increasing function of the density.

Figure 17 shows the ratio $\omega(r) = p(r)/\rho(r)$, which is again a result of the numerical solution and exhibits behavior similar to the polytropic case. Additionally, the mass function profile $m(r)$, shown in figure 18, becomes constant for radii greater than the star's radius, i.e. in the exterior of the spherical object.

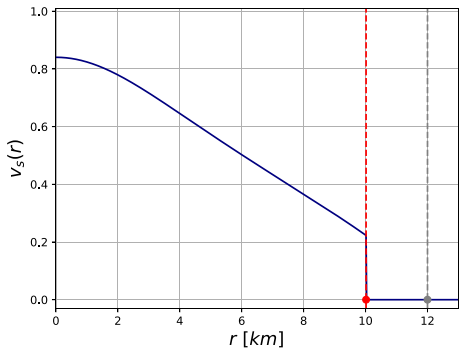

(a) Sound speed in model 3.

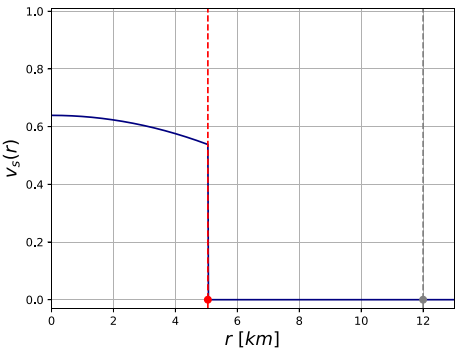

(b) Sound speed in model 4.

Figure 15. Sound speed inside the star $v_s(r)$ for the two models presented in table 2. The red and gray vertical dashed lines represent the radius of zero pressure and the radius of the star, respectively.

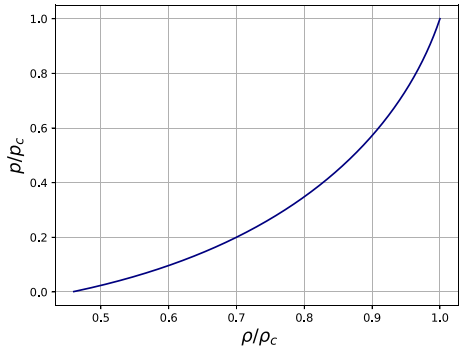

(a) Equation of state for model 3.

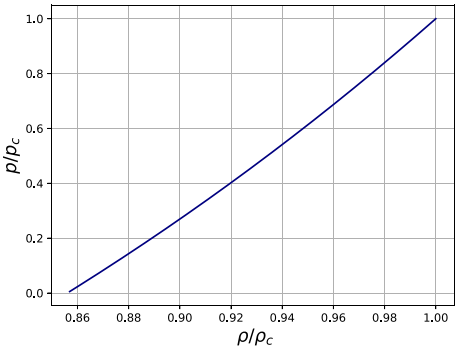

(b) Equation of state for model 4.

Figure 16. Equation of State. Pressure p as a function of the total energy density ρ for the two models presented in table 2.

Finally, the metric functions $A(r) = \mathrm{e}^{2\psi(r)}$ and $\mathrm{e}^{2\phi(r)}$ are shown in figures 19 and 20. Considering the metric function $A(r)$, we observe that both cases satisfy the Buchdahl condition given in (26). Additionally, both metric functions correctly match the Schwarzschild solution beyond the star radius.

5.1. Mass-to-radius relation

The mass-to-radius relationship for the model presented here can be obtained analytically from equation (14) and is given by

$$M = 4\pi R^3 \left[\frac{\rho_c}{3} - \frac{c_2 R^2}{5} - \frac{c_4 R^4}{7} \right] . \tag{28}$$

The explicit dependence of this polynomial function on the values of the constants ρ_c, c_2, and c_4 can, in principle, be very intricate. However, using equation (13) which relates these

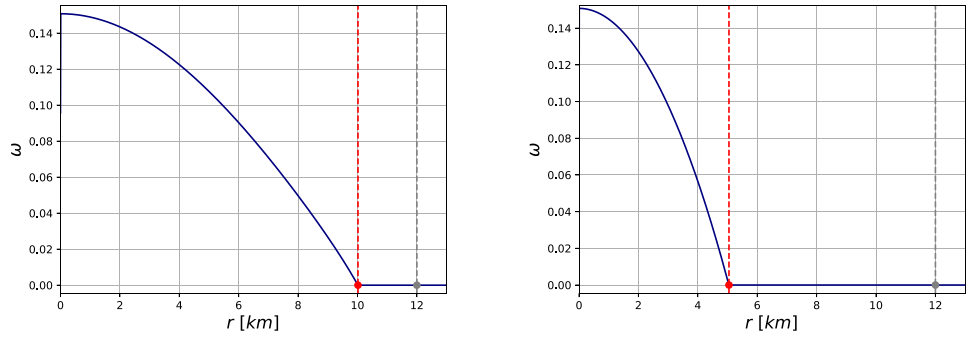

(a) Ratio of pressure to density for model 3. (b) Ratio of pressure to density for model 4.

Figure 17. Ratio between the pressure and the total energy density, $\omega(r) = p(r)/\rho(r)$, for the two models presented in table 2. The radius of the star is shown as a vertical gray line.

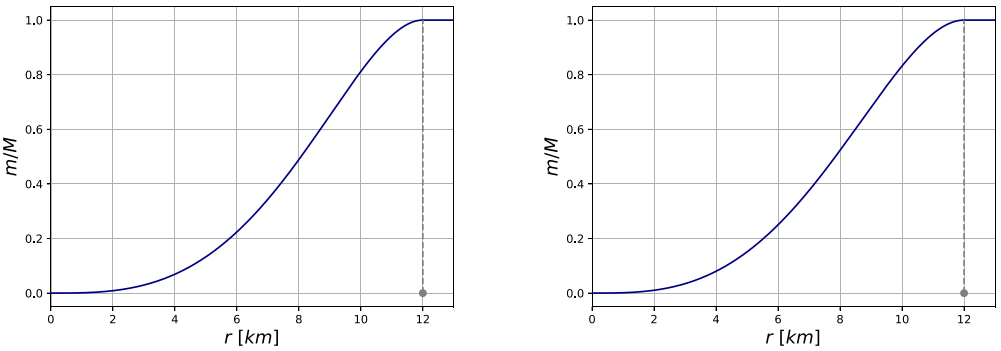

(a) Mass function for model 3. (b) Mass function for model 4.

Figure 18. Mass function $m(r)$ for the two models presented in table 2. The radius of the star is denoted by a vertical gray line.

three parameters to the total radius R, this relationship becomes quite simple as we can obtain an alternative expression for the total mass M in terms of the radius R

$$M(R) = \frac{8\pi R^5}{105}\left(7c_2 + 10c_4 R^2\right) , \tag{29}$$

which is a positive increasing function of the radius as expected from a physical point of view. From this expression, it follows that by fixing the two parameters c_2 and c_4, we can determine the total mass as a function of the radius. In figure 21, we illustrate the behavior of the above mass-to-radius function for the values of c_2 and c_4 given in table 2. The specific point corresponding to the model 3 (with all three parameters fixed) is highlighted in red. Additionally, the figure also shows a shaded region where the cases that satisfy the Buchdahl limit are located. Notice, however, that since the configurations analyzed in this work can also be used as initial conditions for a gravitational collapse, the unshaded region also represents possible solutions.

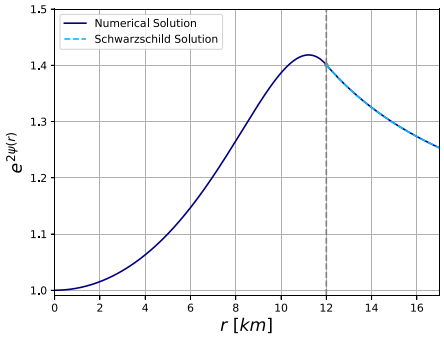

(a) Metric function $A(r) = e^{2\psi(r)}$ for model 3.

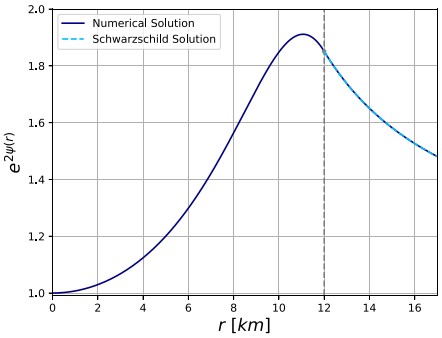

(b) Metric function $A(r) = e^{2\psi(r)}$ for model 4.

Figure 19. Metric function $A(r) = \mathrm{e}^{2\psi(r)}$ for the two models presented in table 2. The radius of the object is shown in gray.

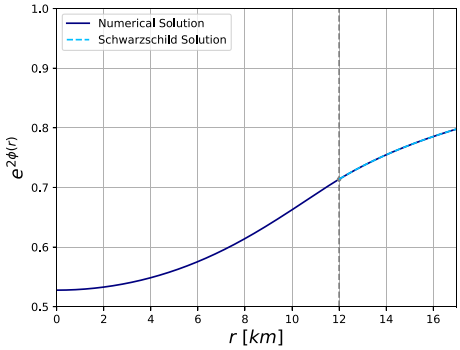

(a) Metric function $e^{2\phi(r)}$ in model 3.

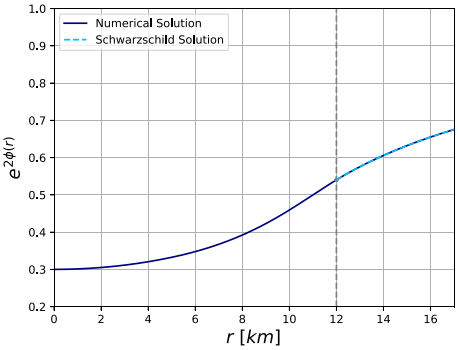

(b) Metric function $e^{2\phi(r)}$ in model 4.

Figure 20. Metric function $\mathrm{e}^{2\phi(r)}$ for the two models presented in table 2. The radius of the star is represented by the vertical gray line.

Table 3. Total mass in kilometers, kilograms, and solar masses for the two cases presented in table 2.

Total mass	(km)	(kg)	$[\mathrm{M}_\odot]$
Model 3	1.72	2.31×10^{24}	1.16
Model 4	2.76	3.72×10^{24}	1.86

In the case of the two specific models discussed in the previous section, the total mass M is presented in different units in table 3. In both cases, the masses are comparable to the solar mass $M_\odot = 1.48$ km. This shows that our approach leads to solutions that represent compact objects with realistic values for the mass and radius.

To illustrate the behavior of the mass function (29) in figure 21, we have chosen a specific combination of the parameters, which correspond to realistic objects, as shown in the previous section. However, many other combinations of the parameters are possible. To illustrate other

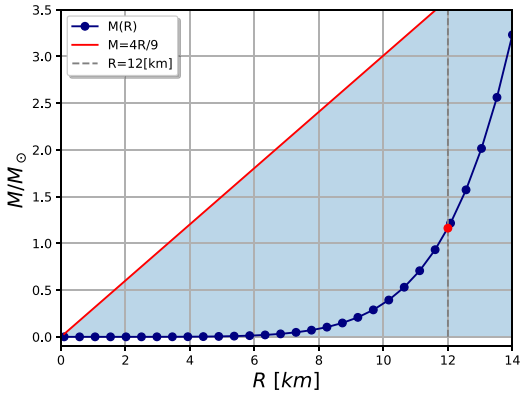

Figure 21. The mass-to-radius function for the parameters $c_2 = 8.55 \times 10^{-7}$ and $c_4 = 1.59 \times 10^{-8}$. Each blue dot can be interpreted as a compact object with the corresponding values of total mass and radius. All the objects have the same kind of matter since all the three parameters of the density profile are fixed. The red dot denotes the object of model 3 (see table 2). The red right line represents the Buchdahl limit.

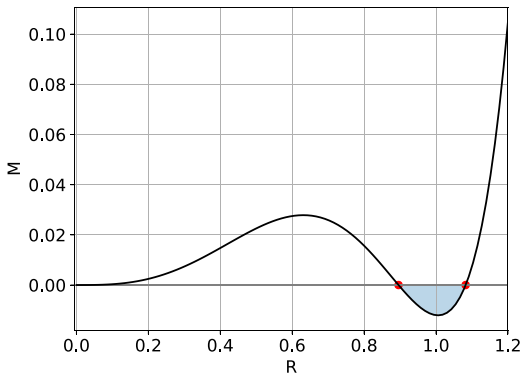

Figure 22. The mass-to-radius function (28) with parameters $4\pi\rho_c = 1$, $c_2/\rho_c = 3.5$, $c_4/\rho_c = -2.5$. The shaded region represents non-physical solutions with negative masses.

possibilities, we plot in figure 22 the mass function (28) with a particular parameter combination, which leads to a region with non-physical negative masses. This means that not all the solutions that follow from the integration of the field equations are allowed. One could wonder if the solutions represented by the red points (objects with zero mass) are allowed. One can easily show that such solutions are also not allowed because on the red points and close to them the density of the objects, according to equation (12), becomes negative.

From the above analysis, we conclude that models 3 and 4 can be used to describe neutron stars in the sense that the resulting values for the masses and radii are comparable with the observed values for this kind of compact objects. In the case of models 1 and 2 of the previous section, we were able to derive effective EoSs that allowed us to identify the internal physical structure of the objects, namely, as polytropic-like and barotropic-like matter, respectively. In the case of models 3 and 4, this approach would not allow an appropriate identification of the corresponding EoS. This is so because in our method, the effective EoS is determined

numerically by only two parameters, c_2 and c_4, whereas in the case of neutron stars, there exist a large number of possible EoS, which contain many parameters that take into account nuclear, thermodynamic, and other properties of the matter inside the star. In principle, in our approach, it should be possible to take into account the internal properties of the star by considering the parameters c_2 and c_4 as depending effectively on the parameters that characterize the nuclear, thermodynamic, and other internal properties of neutron stars. This task, however, is well beyond the scope of the present work in which we focus on the proof of principle of our approach.

5.2. Limiting models

We will show here that it is possible to find limiting models with small dust layers. To this end, we keep the following three parameters fixed: the radius of the object $R = 12\,\text{km}$, the central rest energy density $\rho_c = 2.87 \times 10^{-4}\,\text{km}^{-2}$, and the central pressure is $p_c = 4.33 \times 10^{-5}\,\text{km}^{-2}$ (these values come from the examples of the previous section). Then, we choose the values of the parameters c_2 and c_4 for which the thickness of the dust layer tends to zero. This is reached for the values:

$$c_2 = 3.27 \times 10^{-6}\,, \qquad c_4 = 1.42 \times 10^{-9}\,. \tag{30}$$

The resulting solutions are shown in figures 23 and 24. Both the total and rest mass energy densities, as well as the pressure, decrease monotonically. The pressure reaches zero at a radius $r = 11.95\,\text{km}$, resulting in the thinnest possible dust layer with a thickness of 0.05 km. Furthermore, when we try to reduce the size of the dust layer, the numerical data produce models with a core radius tending to zero, pointing out a breakdown of the approach in the case of very small dust layers.

For the thinnest possible dust layer, the behavior of the sound speed, as shown in figure 23(c), has a central and maximum value of $v_s = 0.47$. In general, we see that all the functions show a behavior analogous to the plots presented in the previous sections. This shows that the presence of a dust layer around the central core facilitates the numerical integration of the model, but it is not necessary for the construction.

6. Stability and convergence

To test the stability of the model presented here, we varied the five parameters given in tables 1 and 2 by a factor of 0.5%. The resulting relative errors are presented in figures 25 and 26 for the models of section 4 and the neutron star models, respectively. We observe that the maximum relative error in the models of the section 4 is of the order of 10^{-3} specifically for the rest energy density. This indicates that the algorithm maintains high accuracy under small perturbations of the parameters, with the rest mass energy density being the most sensitive quantity to these changes.

To study the convergence of the numerical solutions the Hamiltonian constraint is a frequently used tool as shown, for example, in [9]. However, in our case, this is satisfied exactly, as its expression

$$\frac{\mathrm{d}A}{\mathrm{d}r} = A\left[\frac{1-A}{r} + 8\pi r A\rho\right]\,, \tag{31}$$

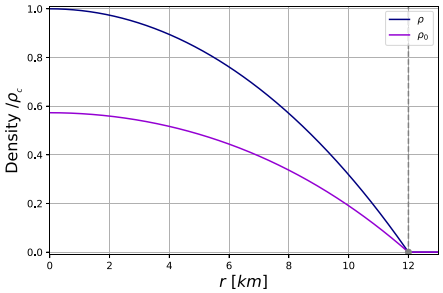

(a) Total energy density.

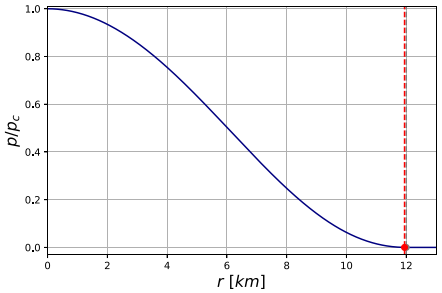

(b) Pressure.

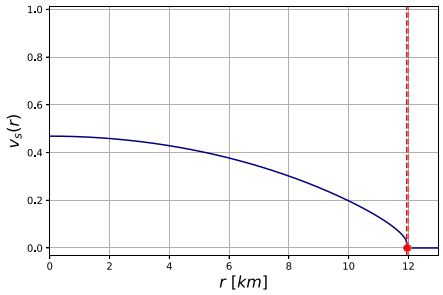

(c) Sound speed.

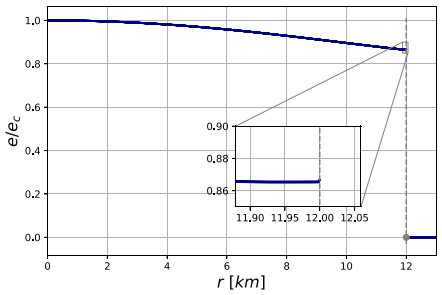

(d) Specific internal energy.

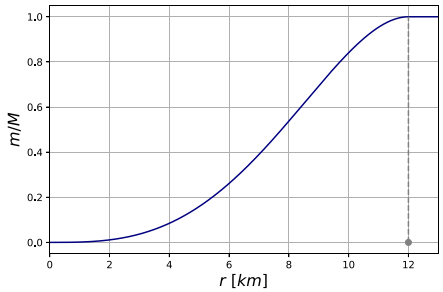

(e) Mass function.

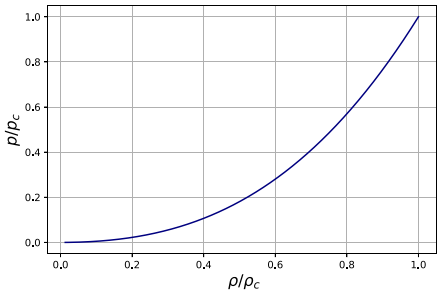

(f) Equation of state.

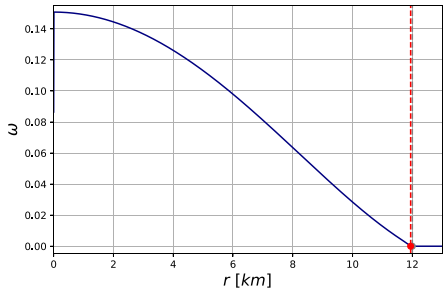

(g) Barotropic function $\omega = p/\rho$.

Figure 23. Neutron star model.

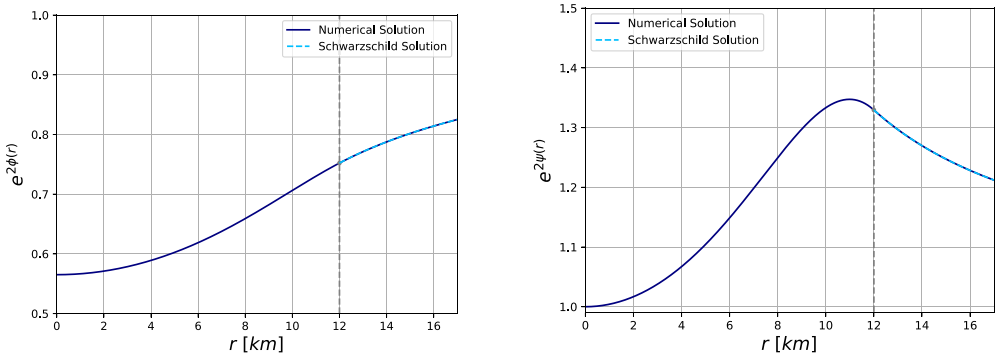

(a) Metric function $e^{2\phi(r)}$. (b) Metric function $e^{2\psi(r)}$.

Figure 24. Metric functions $\mathrm{e}^{2\phi(r)}$ and $A(r) = \mathrm{e}^{2\psi(r)}$. The radius of the object is shown in gray.

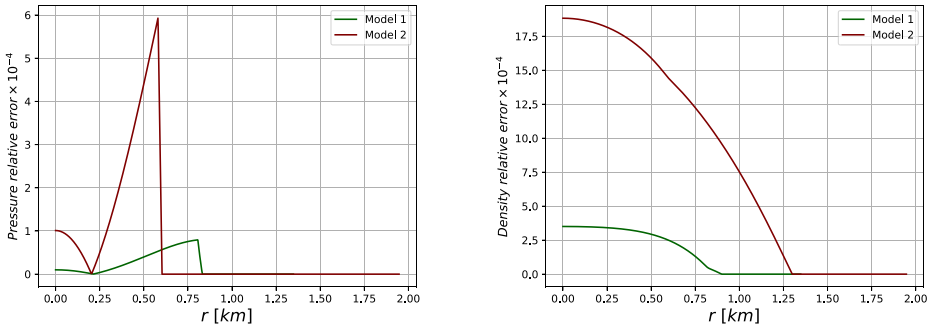

(a) Relative error of the pressure p for the models of the section IV.

(b) Relative error of the rest energy density ρ_0 for the models of the section IV.

Figure 25. Relative error for the models of section 4 given in table 1 when the parameters are modified by 0.5%.

can be derived without the numerical solution. This is because all functions are fixed analytically. The metric function $A(r)$ is given by the expression (15) and the total energy density is given by (12). In fact, the demonstration is immediate and we find

$$\frac{\mathrm{d}A}{\mathrm{d}r} = \begin{cases} 16\pi\, rA\,(r)^2 \left[\frac{1}{3}\rho_{\mathrm{c}} - \frac{2}{5}c_2 r^2 - \frac{3}{7}c_4 r^4\right] , & r < R \\ -\frac{2M}{(r-2M)^2} , & r > R\,. \end{cases} \tag{32}$$

Therefore, in order to study the convergence we use the standard numerical recipes. Specifically, we varied the value of the step size Δr and observed the resulting convergence order using a reference solution for the pressure with $\Delta r_{\mathrm{ref}} = 1 \times 10^{-5}$. The numerical method (RK4) is of fourth order; thus, the error in the pressure should decrease by a factor of $2^4 = 16$, when the step size is halved. We calculate the L_∞ norm of the difference between the reference solution and the solutions obtained by systematically reducing the mesh size. As a result, we obtain the set of plots shown in figures 27 and 28, which show explicitly the convergence of our numerical solutions.

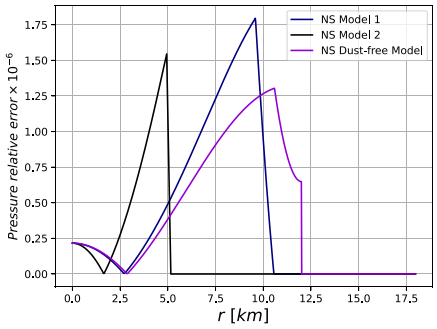

(a) Relative error of the pressure for the neutron star cases.

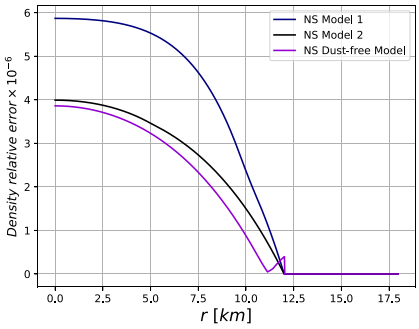

(b) Relative error of the rest mass energy density for the neutron star cases.

Figure 26. Relative error for the neutron star cases given in table 2 when the parameters are modified by 0.5%.

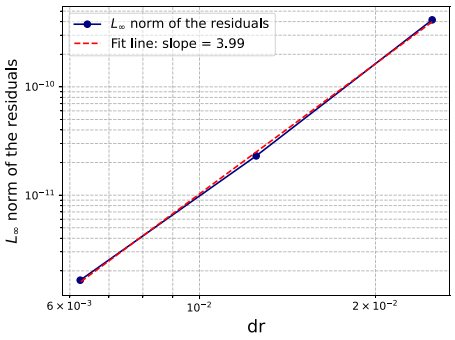

(a) Convergence for model 1 of section IV.

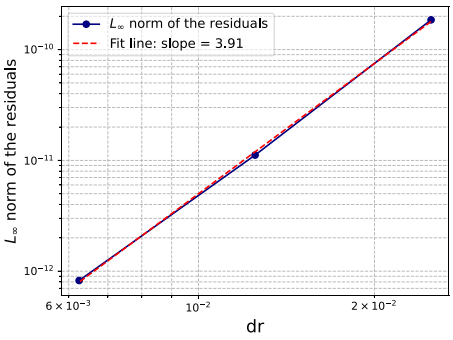

(b) Convergence for model 2 the section IV.

Figure 27. Convergence of the RK4 method for the models of the section 4. The L_∞ norm of the difference between a reference solution and the solutions obtained by systematically reducing the step size Δr is plotted on a logarithmic scale. The slope must be four for a code of fourth order.

7. Conclusions

In this work, we investigated spherically symmetric solutions of the Einstein equations with a perfect fluid as the source of gravity. Although there are many solutions in the literature with these characteristics, we focus on solutions that could be used to describe the gravitational field of realistic mass distributions. To this end, we demand that the solutions are free of singularities inside the fluid, present positive energy and pressure profiles, are in accordance with the Buchdahl limit, and are such that the sound speed satisfies the light speed limit.

To solve the above problem, an EoS is usually given *a priori* that is commonly taken as a barotropic or a polytropic EoS. Our approach is different. We begin with a predetermined energy density profile, given as a polynomial function of the radial coordinate with arbitrary coefficients, which can be fixed in such a way as to guarantee that the energy density is consistent with the physical expectations. In particular, we study profiles in which the energy is

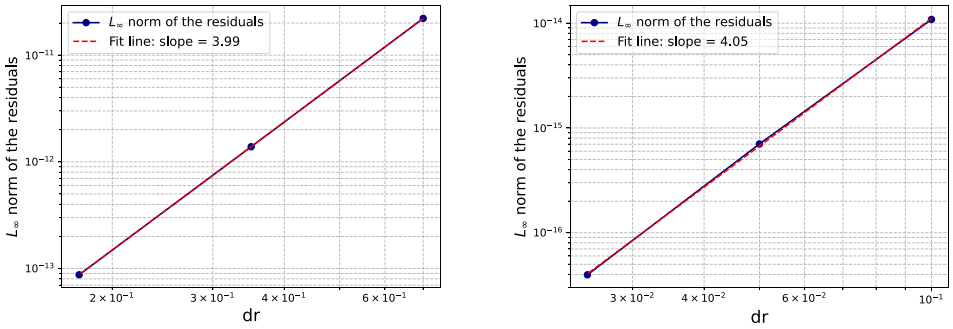

(a) Convergence of the model 1 for neutron stars. (b) Convergence of the model 2 for neutron stars.

Figure 28. Convergence of RK4 method for the neutron star cases. The L_∞ norm of the difference between a reference solution and the solutions obtained by systematically reducing the step size Δr is plotted on a logarithmic scale. The slope must be four for a code of fourth order.

a decreasing function of the radial distance with its maximum at the center and its minimum (vanishing density) at the radius of the star. We show that the properties of the resulting models are essentially determined by a set of parameters that correspond to the values of the energy density and pressure at the center of the object and two constants that determine the energy density profile.

We solve the TOV equations to determine the pressure profile and the metric functions, imposing the physical conditions mentioned above. It turns out that the configurations that agree with all physical requirements consist essentially of a central core surrounded by a layer of dust, whose thickness depends on the values chosen for the central pressure and the energy density profile. Moreover, we argue that dust layers surrounding compact objects have already been observed in Pleiades stars, red giants, and main-sequence stars, thus showing the applicability of our approach in realistic configurations.

First, we test our approach in two different cases, in which the values of the parameters determining the model are chosen arbitrarily within the intervals allowed by the physical requirements. As a second example, we consider two cases with parameter values fixed by the physical properties of canonical neutron stars. This shows the physical consistency of our approach.

Although our approach is not based on a particular EoS that determines the internal properties of the object, we can derive effective EoSs and verify their physical significance by comparing their behavior with the properties of known EoSs. We prove that compact objects described within our model 1 can be interpreted as having a polytropic-like structure. In contrast, model 2 leads to an internal structure characterized by a barotropic-like EoS. In the case of models 3 and 4, it is shown that they produce values for the mass and radius of compact objects that are comparable with the values observed for neutron stars. We interpret these results as a proof of principle of the applicability of the approach proposed in this work.

In addition, we tested the stability and convergence properties of our numerical solutions by using standard criteria for numerical methods. As for the stability test, we varied the five parameters given in tables 1 and 2 by a factor of 0.5% and found that the maximum relative error is of the order of 10^{-3} for the rest mass energy density. We conclude that the algorithm maintains high accuracy under small changes in the parameters.

To study the convergence we varied the step size of the numerical mesh Δr and analyzed the resulting convergence order for the pressure using a reference solution with $\Delta r_{\text{ref}} = 1 \times 10^{-4}$. The numerical method RK4 has an expected convergence factor of $2^4 = 16$ when the step size is halved, as we observe when we calculate the $L_i nfty$ norm of the difference between the reference solution and the solutions obtained by systematically reducing the mesh width. This proves explicitly the convergence of our approach.

The model presented here can be used as the initial state for the study of the gravitational collapse of spherically symmetric mass distribution by using the tools of numerical relativity. Since the behavior of the physical quantities involved in the model can be controlled by choosing the parameters of the perfect fluid and pressure, we expect that a similar procedure could be used to control the dynamical evolution of the collapse. In particular, the dust layer, which surrounds the central core of the object in our model, seems to be an appropriate initial state for gravitational collapse since the dust should collapse under the sole action of the gravitational field of the central core. We expect to study the dynamical collapse of our models in future works.

Data availability statement

All data that support the findings of this study are included within the article (and any supplementary files).

Acknowledgments

This work was partially supported by CONACyT Network Project Nos. 376127, 304001, and DGAPA-UNAM Project IN100523. The work of HQ was supported by DGAPA-PAPIIT-UNAM, Grant No. 108225.

ORCID iDs

Elly Bayona https://orcid.org/0000-0001-7758-6407
Hernando Quevedo https://orcid.org/0000-0003-4433-5550
Miguel Alcubierre https://orcid.org/0000-0003-3367-9868

References

[1] Thorne K S, Misner C W and Wheeler J A 2000 *Gravitation* (Freeman)
[2] Delgaty M and Lake K 1998 *Comput. Phys. Commun.* **115** 395
[3] Stephani H 2004 *Relativity: An Introduction to Special and General Relativity* (Cambridge University Press)
[4] Nambo E C and Sarbach O 2021 Static spherical perfect fluid stars with finite radius in general relativity: a review *Rev. Mex. Fis.* E **18** 020208
[5] Buchdahl H A 1959 *Phys. Rev.* **116** 1027
[6] Baumgarte T W and Shapiro S L 1998 *Phys. Rev.* D **59** 024007
[7] Shibata M and Nakamura T 1995 *Phys. Rev.* D **52** 5428
[8] Alcubierre M 2008 *Introduction to 3+ 1 Numerical Relativity* vol 140 (OUP Oxford)
[9] Alcubierre M and Mendez M D 2011 *Gen. Relativ. Gravit.* **43** 2769
[10] Alcubierre M, Barranco J, Bernal A, Degollado J C, Diez-Tejedor A, Megevand M, Núñez D and Sarbach O 2019 *Class. Quantum Grav.* **36** 215013

[11] Degollado J C, Salgado M and Alcubierre M 2020 *Phys. Lett.* B **808** 135666
[12] Press W H, Vetterling W T, Teukolsky S A and Flannery B P 1988 *Numerical Recipes* (Cambridge University Press)
[13] Wheeler J C and Chatzopoulos E 2023 *Astronomy & Geophysics* **64** 3.11–3.27
[14] Jura M 1999 *Astrophys. J.* **515** 706
[15] Aumann H, Gillett F, Beichman C, De Jong T, Houck J, Low F, Neugebauer G, Walker R G and Wesselius P R 1984 *Astrophys. J.* **278** L23
[16] Condon J J and Ransom S M 2016 *Essential Radio Astronomy* vol 2 (Princeton University Press)